Title
Reducing energy cost of NO x production in air plasmas

Permalink
https://escholarship.org/uc/item/8tr9x9ss

Authors
Pei, Xuekai
Gidon, Dogan
Yang, Yao-Jhen
et al.

Publication Date
2019-04-01

DOI
10.1016/j.cej.2019.01.011

Peer reviewed

Reducing energy cost of NO$_x$ production in air plasmas

Xuekai Pei, Dogan Gidon, Yao-Jhen Yang, Zilan Xiong, David B. Graves*

Department of Chemical and Biomolecular Engineering, University of California, Berkeley, CA 94720 USA

HIGHLIGHTS

- Average electric field and average temperature play a key role in efficient nitrogen fixation.
- NO$_x$ production cost across different air discharges can be correlated using a single parameter.
- Reducing the breakdown cost is key method of increasing NO$_x$ production efficiency.
- Extending the discharge length after breakdown remarkably reduces the energy cost of NO$_x$.

GRAPHICAL ABSTRACT
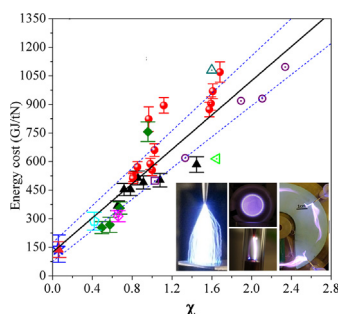
ARTICLE INFO

ABSTRACT

Current worldwide fixed nitrogen utilization efficiency (NUE) is low, leading to significant environmental problems. An important aspect of this problem involves NH$_3$ released from bacterially degraded, N-containing organic waste such as animal manure. Acidifying organic waste with nitric acid traps NH$_3$ as NH$_4$NO$_3$, thus increasing the nitrogen content of the resulting organic fertilizer and reducing the environmental effects of NH$_3$ emission. Air plasmas have been proposed for this purpose through production of NO$_x$ from air which can be readily converted to nitric acid. However, a major challenge remains in reducing the energy cost of NO$_x$ production in air plasmas to make the technology economically competitive. Different types of discharges such as arcs, sparks, dielectric barrier discharges have been investigated for NO$_x$ production but they are challenging to compare due to differences in their structure, geometry and excitation modes etc. Different discharges also utilize potentially different chemical reaction pathways to produce NO$_x$. As of yet, there are no general evaluation criteria to determine the qualities of an appropriate discharge configuration for energy-efficient NO$_x$ production. In this study, we report on four types of discharges; dielectric barrier, glow, spark and extending arc discharge to examine NO$_x$ production efficiency under different conditions. Based on our results and previously published results from the literature, we propose a dimensionless parameter to guide the design of appropriate plasma sources for reduced energy cost NO$_x$ production.

1. Introduction

Reactive (or 'fixed') nitrogen (N_r) is an essential component in synthetic fertilizers and is currently almost exclusively supplied via a chemical synthesis process ('Haber-Bosch,' or HB) originally developed in Germany in the first decade of the 20th century [1–3]. Nitrogen fertilizer generated via HB increased agricultural productivity to sustain nearly half of world population by the late 20th century. Since its inception in 1913, the HB process has been improved and refined. Modern, highly heat integrated HB plants use less than 30 GJ/tN

(gigajoules expended per metric ton nitrogen produced) [4]. This value is remarkably close to the minimum thermodynamic limit of 24 GJ/tN [5,6]. In spite of the obvious advantages of HB fertilizer manufacture, there are several significant problems with utilizing HB-manufactured synthetic fertilizer to meet current and future worldwide demand for N_r. The most important problems are environmental. HB plants and the associated transportation and distribution systems annually emit more than 300 million metric tons of carbon dioxide, about 120 million tonnes of NO_2 and over 80 million tonnes of NH_3 [7,8]. A secondary issue is that the total amount of energy used worldwide by HB manufacture (1–2%), coupled with the likely growth in demand over the next several decades represent a significant potential challenge to world energy supplies. In addition, the near-exclusive use of synthetic fertilizer has discouraged use of organic fertilizer which includes many valuable micronutrients [7,9,10].

Before the HB process was invented in 1913, there were several commercial processes throughout the world that used air plasma to manufacture nitrogen based fertilizers. The best known process was the one developed and commercialized in the early 1900s by the Norwegian team of Birkeland and Eyde [2,11]. After making NO_x in a plasma arc, the gas was dissolved in water to form nitric acid. This nitric acid solution was combined with calcium carbonate (limestone) to make calcium nitrate. This compound was sold as fertilizer. Application of air plasma to directly create synthetic fixed nitrogen fertilizers – the Birkeland – Eyde approach or some variation – would almost certainly not be economically effective today. However, there are ways air plasma technology can *complement* HB without directly competing with it.

This concept has been described previously [12,13], but briefly, the proposed technology utilizes electrically-powered air plasma to create nitric oxide (NO). NO is readily oxidized under atmospheric air conditions to form NO_2. When NO_2 is dissolved in water, primarily HNO_3 (in aqueous phase, nitrate anion NO_3^-) is created. We envision using this aqueous NO_3^- to treat nitrogen-containing organic waste such as manure or urine, lowering the pH to convert otherwise volatile NH_3 to involatile ammonium nitrate (i.e. NH_4NO_3). Volatile NH_3 is naturally created when bacteria break down organic forms of nitrogen in protein nucleic and amino acids. Use of nitric acid *doubles* the N-content of the organic fertilizer since for each molecule of NH_3 retained as NH_4^+, a molecule of NO_3^- is added. [12]. A key requirement for the competitiveness of this technology is the utilization of distributed plants of relatively small scale, located where organic waste is created and powered by locally produced renewable energy sources.

The commercial viability of the proposed technology relies on numerous considerations including the concentration and throughput of produced NO_x, safety, ease of operation, and process economics. The latter consideration relies heavily on the development of discharge configurations with reduced energy cost of NO_x production. Until now there are no generally accepted evaluation criteria to determine the qualities of an appropriate discharge configuration for energy-efficient NO_x production. We therefore focus our efforts on this question. The mechanisms of NO_x formation in air plasma have been studied for many years in the context of atmospheric lightning discharge [14–21]. More recently, several non-thermal plasma sources have been considered for nitrogen fixation [22–34]. These non-thermal sources are attractive as they typically have lower power requirements and are easier to operate. Furthermore, Cherkasov et al., estimate nitrogen fixation with non-thermal sources can theoretically reach comparable energy efficiency with HB [2]. Various non-thermal plasma sources have been invested for NO_x production with reported energy costs no lower than about 100–200 GJ/tN [22–34]. It should be noted that a direct comparison of only energy cost per mass N_r created is not necessarily the proper metric to judge the potential attractiveness of the proposed technology. The technology must be economically competitive of course, but it must also satisfy many other constraints such as impact on the environment, appropriateness for a given local area and other factors.

Notable non thermal plasma sources proposed for NO_x production include dielectric barrier discharge (DBD), glow, spark and arc type of discharges [28,30,29]. For example, Patil et al. [28] investigated a packed bed DBD reactor combined with different catalysts to increase the produced NO_x concentration. The reported energy efficiency of NO_x synthesis for this configuration is about 4500 GJ/tN without catalyst. They also reported that oxygen activation plays a minor role in plasma catalytic nitrogen fixation under their studied conditions. Janda et al. [30] reported a pin-to-plane atmospheric air transient spark discharge, driven by a DC power supply to generate NO_x. They reported the energy cost of 614 GJ/tN for NO_x production. Wang et al. [29] investigated a pulsed-power gliding-arc reactor operating at atmospheric pressure for nitrogen oxide synthesis and developed a chemical kinetics model for this discharge. They proposed that vibrational excitation of N_2 in the gliding arc contributes significantly to activating the N_2 molecules to enable the key reactions leading to NO formation. These authors observed an energy cost for NO_x formation of about 300 GJ/tN. The fact that the 'warm' gliding arc discharge was shown to be more efficient than the 'cold' DBD discharges has hints for some of the key mechanisms in creating NO_x in these types of discharges. Burnette et al. [35], investigated the nitric oxide kinetics in the afterglow of a nanosecond-pulsed discharge to gain insight into the mechanisms of NO_x production. They argue that the increased stability of the discharge with short pulse duration as well as the high reduced electric field during the pulse make this type of discharge suitable for increased molecular dissociation. Other researchers also have reviewed and compared different kinds of plasma sources for nitrogen fixation [5,2,31]. It is, however, challenging to compare these discharges, since under different conditions discharge properties (structure, discharge mode, current profiles etc.) drastically vary. The chemistry involved in NO_x production is also complex. Different reaction pathways may become dominant under different conditions. To date, there appears to be no general evaluation criteria to guide the design of an appropriate discharge configuration for this application.

In this study, we investigate four different types of discharges (DBD, glow, spark and arc type) in order to identify key parameters affecting the energy cost for NO_x production and to guide design rules for discharge structures with improved performance. We first present the experimental set-ups and measurement methods we utilized in the study, followed by results regarding energy cost of NO_x production under different discharge conditions. Finally we present a dimensionless parameter that appears to correlate energy cost of NO_x production with a range of different discharges. One of the key novel results of the paper is the identification and discussion of the importance of this dimensionless parameter involving the average electric field and the average gas temperature in the discharge. This parameter seems to correlate with the overall energy efficiency of various types of discharges in creating NO_x, although the underlying physico-chemical mechanisms responsible for this correlation are not fully understood at present.

2. Experimental setups and measurements

2.1. Experimental setups

We investigate four different discharges in air: DBD, pin-to-plane DC glow, pin-to-plane nanosecond-pulsed spark discharge and an extending arc (Propeller Arc (PA)) discharge. The experimental setups and photos corresponding to each of these discharges are as shown in Fig. 1. These four atmospheric pressure, non-equilibrium discharges represent a cross-section of typical types of sources used for NO_x production, however they have significant differences in their characteristics including electrical characteristics, gas temperature, electron temperature, electron density, etc. [36] The key characteristics of the four discharges investigated in this study are summarized in Table 1.
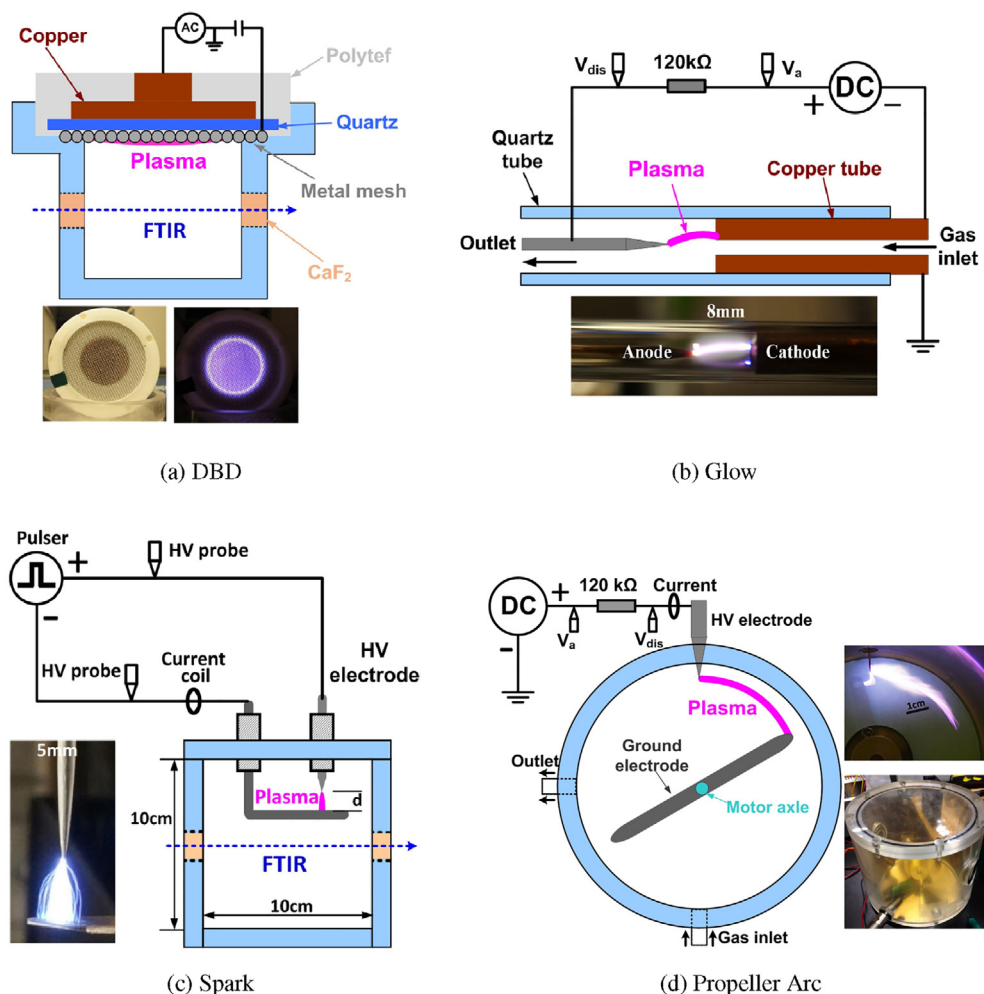
(a) DBD

(b) Glow

(c) Spark

(d) Propeller Arc

Fig. 1. Configurations and photos of experimental setups for NO_x production for (a) DBD, (b) glow discharge, (c) spark discharge and (d) PA discharge.

Table 1
Summary of key characteristics of the four discharges investigated in this study.

Discharge	DBD	Glow	Spark	PA
Excitation	AC	DC	ns-pulsed	Self-pulsed
Frequency	25 kHz	N/A	1 kHz	45 Hz
Flow	Batch	2 L/min	Batch	3 L/min
Geometry	Surface Discharge	Pin-to-Plane	Pin-to-Plane	Stretching

2.1.1. DBD

Fig. 1a shows the schematic of DBD also termed Surface Micro-discharge (SMD). This setup has been studied in previous work [37–40]. The DBD consists of a cylindrical copper block (47 mm in diameter), used as the powered electrode, covered by a thin quartz plate (1 mm in thickness), which functions as a dielectric barrier. A wire mesh with a diameter of 0.5 mm and a mesh density of 88 meshes per cm^2 is situated on the quartz plate and used as ground electrode. The electrodes are placed within a cylindrical acrylic enclosure (46 mm in height and 50 mm in diameter) to confine the reactive species produced by the plasma. There are two infrared-transparent windows (Calcium Fluoride CaF_2, Edmund Optics) in the acrylic enclosure situated 2 cm below the electrode. The DBD device is powered by a custom-made high-voltage alternating current (AC) power supply producing 0–20 kV at 20–60 kHz. The photographs of the DBD device and the discharge are also presented in the Fig. 1a.

2.1.2. Glow discharge

The DC glow discharge has simple pin-to-plane configuration. Fig. 1b shows the configuration of the experimental set up for the DC glow discharge as well as a photo of a typical discharge condition with the gap distance set to 8 mm. The electrodes are situated in a quartz tube (ID 5 mm, OD 7 mm). A mass flow controller (UFC-1500A, 0–3 slm) is used to maintain a constant flow rate of 2 L/min of bottled compressed-air (PRAXAIR INC) via a PTFE gas line. A copper tube (ID 3 mm, OD 5 mm) is used as the cathode which doubles as the gas flow channel and fits flush inside the quartz tube. A tungsten needle, connected to the positive pole of a HV DC power supply (Spellman High Voltage, SL10PN1200) through a ballast resistor (120 kΩ), is used as the anode. Here, the ballast resistor limits the discharge current below 120 mA, which is the highest current rated for the DC power supply. In this configuration, the gas flow also serves to cool the device allowing for more stable operation. The generated NO_x is driven into a standard gas cell (Bruker, A132-2) with 20 cm path-length which is placed inside the infrared spectrometer. The Fourier Transform Infrared (FTIR) spectroscopy signal is collected after 5 min of stable discharge. Details of FTIR measurements are presented in the following sections.

2.1.3. Spark discharge

The pin-to-plane discharge configuration is depicted in Fig. 1c. A tungsten pin with a diameter of 1.6 mm is used as the anode and a copper plate (10 mm × 100 mm) serves as the cathode. The separation distance d between the pin tip and copper plate can be manipulated precisely through a threaded adjuster. Photographs of the typical

discharge at d = 5 mm is also shown in Fig. 1c. The pin-to-plane discharge is driven by a nanosecond pulsed power supply (NSP-100, EHT) with a floating output stage. The power supply is capable of generating voltage amplitudes of up to 20 kV with a repetition rate up to 10 kHz, and a variable pulse width from 40 ns to 260 ns. These conditions correspond to the discharge operating in a spark-like mode [36,41]. An acrylic chamber is used to confine and measure the chemical species produced by the pin-to-plane discharge (see Fig. 1c). The acrylic chamber measures 100 × 100 × 100 mm (or 1 L) in volume, with the electrodes mounted on the lid. Two infrared-transparent windows are placed on parallel sides of the box for spectroscopy measurements.

2.1.4. The Propeller Arc

Fig. 1d shows the configuration of the extending-arc type source we termed 'Propeller Arc' (PA). The basic characteristics of the PA are investigated in [42]. Briefly, the PA consists of a rotating cathode (ground electrode), driven by a motor, with a fixed anode (HV electrode). Two propeller-like blades of cathode are made of stainless-steel. The distance between the center of motor axis and the tip of cathode is 35 mm. A stainless-steel pin with a diameter of 0.8 mm is used as the anode. Using the DC power supply (Spellman High Voltage, SL10PN1200), PA discharge can be extended up to a length of 82 mm as the cathode rotates, as shown in Fig. 1d. The motor speed is maintained at 1350 rpm, corresponding to a discharge frequency of 45 Hz. Note here that since the propeller has two blades, discharge frequency is twice that of the rotor. A ballast resistor in series is used to limit the current. The PA discharge is situated inside an acrylic cylindrical chamber with an inner diameter of 100 mm and a height of 100 mm (see Fig. 1d). As the glow discharge (see Section 2.1.2), a gas flow system is used to measure NO_x concentration via FTIR. A constant inlet gas flow rate of air or N_2 is maintained at 3 L/min via a MFC. An additional MFC is used to adjust O_2 flow, in order to manipulate the N_2/O_2 ratio.

2.2. Measurement and methods

We use common methods in analyzing the NO_x (including NO, NO_2, HONO) concentration, power consumption, average electric field and gas temperature for the different discharges. We detail each of these methods below.

2.2.1. FTIR measurement

FTIR spectroscopy is performed as an in situ diagnostic for NO_x concentration in the different discharge configurations. For the DBD and pin-to-plane spark discharge, the devices are placed inside the infrared spectrometer (Bruker, Vertex 70) such that the infrared beam passes through the CaF_2 windows placed on the walls of the acrylic chambers. The chambers are operated as batch reactors during FTIR spectroscopy measurements, with no flow of gas allowed between the inside of the chamber and the ambient air. Following each experiment, the chamber was opened and vented inside a fume hood and purged with nitrogen before refilling with ambient air for the next operation. The absorption FTIR spectra are recorded over time after discharge ignition.

In order to avoid the saturation of the FTIR signal with high concentration of NO_x produced in the DC glow discharge and PA discharge, a gas flow system is utilized. An MFC maintains a constant gas flow into the discharge chamber and the gas is driven into a standard FTIR gas cell with 20 cm path-length which is placed inside the infrared spectrometer. The absorption FTIR spectra are recorded after stabilization of the signal. The wavenumber resolution of the measurements is set as 0.5 cm^{-1}, and 32 scans are averaged to create each spectrum. The absolute concentrations of different species (NO, NO_2) are determined by comparing the measurements to calibration data generated using precision calibration gas mixtures (GASCO LLC). Known concentrations of NO and NO_2 in N_2 were added to the standard gas cell for calibration. The FTIR sensitivity to these known gas concentrations was recorded

and used to quantify subsequent measurements. The HITRAN database (http://hitran.iao.ru/) was used for HONO calibration.

2.2.2. Power and energy cost

The power consumption of DBD is measured by the Lissajous method using a 100 nF capacitor inserted in the ground line. The applied voltage is measured using a high voltage (HV) probe (Tektronix P6015A). A differential HV probe (Tektronix P5200A) was used to measure the voltage across the 100 nF capacitor. The power consumption of DBD is calculated by

$$P_{dis} = f \int V_d C dV_c. \tag{1}$$

Here, f is the applied AC frequency (25 kHz), V_d is the measured voltage across the DBD, C is the capacitor capacitance (100 nF), V_c is the voltage across the capacitor.

For the other three discharges, the potential drop across the discharge gap and current are measured separately to calculate the consumed power. The discharge current is measured by a current coil (Pearson 2877) and the power consumption of the discharge is calculated by

$$P_{dis} = f \int_0^\tau V(t) I(t) dt. \tag{2}$$

Here, f is the discharge frequency, $V(t)$ is the gap voltage, $I(t)$ is the discharge current and τ is the discharge pulse-width. All the HV probes and current coils are linked to a 200 MHz digital oscilloscope (Tektronix TDS2024) with a sampling rate up to 2 GHz. It should be noted that the propagation time delay for different probe or coils is on the order of nanoseconds. This delay is found to have significant effects on current measurements for the nanosecond-pulsed discharge configuration and was corrected for in the power calculations. The corresponding voltage-current information reported are also corrected for this time delay.

Using the power and concentration information (see Section 2.2.1), the energy cost of NO_x production is calculated as follows:

$$E_{N_r} = \frac{P_{dis} \times t}{\frac{V}{24\,L/mol} \times c_{NO_x} \times 10^{-6} \times 14\,g/mol} \times 10^{-3}. \tag{3}$$

Here, E_{N_r} is energy expended per unit of reactive N_r (including NO, NO_2, HONO in this paper) expressed in units of GJ/tN. P_{dis} is the plasma power consumption (W), t is time (s), V is the volume of chamber (L) or the volume of gas flow into the chamber, c_{NO_x} is the concentration of NO_x (ppm), 24 L/mol is the molar volume of ideal gas at 1 atm, 293 K, and 14 g/mol is the molar mass of N atom. The factor of 10^{-3} arises from conversion of J/g to GJ/tN.

2.2.3. Average electric fields

In order to further understand the NO_x production process, the average electric fields $\overline{E}$ of the discharges are defined as:

$$\overline{E} = \frac{\int_{t_{bre}}^\tau \frac{V_{dis}(t)}{d} dt}{\tau - t_{bre}}, \tag{4}$$

where $V_{dis}(t)$ is the instantaneous gap discharge voltage and d the instantaneous visible length of the plasma. t_{bre} is the gap breakdown time. This parameter is crucial for the ns-pulsed spark discharge. τ is the discharge pulse-width. For the spark and DC glow discharges, d is constant and equals the gap distance. However for the PA, where the discharge extends during operation, the instantaneous value of d is estimated by,

$$d = t \times f \times L. \tag{5}$$

Here, t is time elapsed after breakdown (s), f is the discharge frequency (in Hz, determined by the motor angular velocity) and L is the half-circle arc length of the propeller-like blade cathode. The latter value equals $\pi \times 3.5 = 11$ cm. The value of d is verified by the time-

resolved high-speed photography. More detailed discussion regarding the PA can be found in [42].

2.2.4. Gas temperature estimation

Optical emission spectra from the N_2 second positive system are simulated and fitted to the measured optical emission spectra (OES) (via SpecAir software) to estimate rotational and vibrational temperatures of nitrogen [43]. The light emitted by the discharge is collected via an optical fiber. The OES spectra are recorded with a USB2000 (Ocean Optics) spectrometer. The integration time is set to 200 ms and the resolution is 0.35 nm/pixel. Note that the gas temperature estimated this way represents a temporally averaged value; we therefore denote it with $\overline{T}$ in units of K.

3. Results and discussion

In this section, we first report results on energy cost of NO_x production with each of the four investigated discharges in corresponding subsections. The analysis of NO_x production for each discharge is carried out based on the unique properties of the discharge. For the DBD, which is a surface discharge, the effect of the mesh material is investigated for potential catalytic properties and results are reported on a per surface area basis. For the DC glow discharge, the transient behavior of the voltage and current is neglected as they are constant through the operation. The effect of the discharge current and gap distance on energy cost of NO_x is investigated. For the ns-pulsed spark discharge, the transient behavior of the discharge throughout the pulse has key implications on discharge properties. The pulse width is varied to gain insight on the discharge behavior in relation to energy cost of NO_x production at different times. The effect of different applied voltages and separation distances are also investigated. Finally, for the PA, the effect of discharge current is investigated as the most significant parameter impacting the energy cost of NO_x production. Moreover, the effect of the composition of the working gas in improving the energy cost of NO_x production is tested with the PA.

In the following subsections, we demonstrate how these seemingly-disparate discharge conditions can be analyzed using a simple, easy-to-measure parameter. We demonstrate that this parameter is capable of capturing our results as well as previously reported results in the literature. Finally we discuss the implications of our analysis in aiding future design of discharge configurations for energy-efficient NO_x production.

3.1. NO_x production by DBD

DBD is a surface discharge whose properties are determined on per discharge area basis. Therefore, we investigate energy cost as a function of power density. The discharge area is equivalent to that of the copper block electrode (diameter of 47 mm). DBDs are known to exhibit two distinct modes based on the dissipated power density [40]. Under low power density, the main reaction product is O_3, and minimal NO_x is produced. We therefore focus on the higher power densities associated with the so-called NO_x mode, where main reaction products are nitrogen oxides. We investigate the effect of increasing power density on NO_x production as well as the effect of the material of the mesh ground electrode.

Fig. 2 shows the temporal evolution of gas-phase NO_x concentrations by DBD configuration with a stainless steel mesh. In Fig. 2, the species concentrations are observed to saturate after 150 s. In this case, the sealed chamber (volume: 0.09 L) impedes the production of NO_x. The concentration of N_2O, which is not useful for nitrogen fixation, reaches the highest concentration of all the produced species after about 150 s. We see the increase of total NO_x concentration is approximately linear over the initial 150 s. This period can be used to estimate the production rate of NO_x based on the slope of this linear trend as shown in solid black line in Fig. 2. For the DBD, the NO_x species
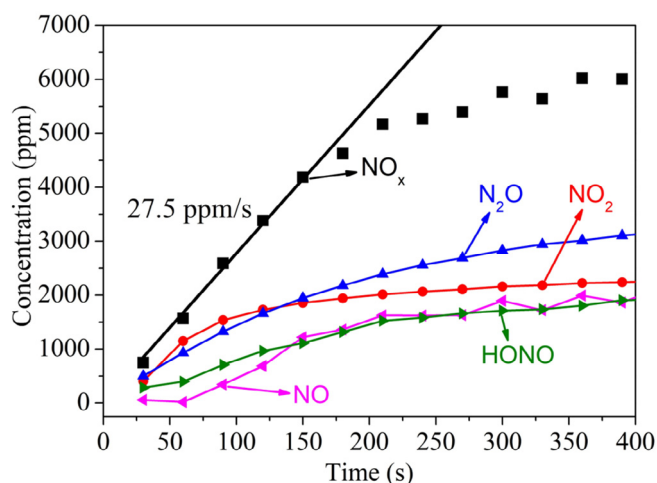

Fig. 2. Measured time-evolution of concentrations of produced NO_x species using DBD, power consumption of 8.64 W (applied peak-to-peak voltage of 9.5 kV at 25 kHz). The confidence intervals for the reported concentrations are approximately ±50 ppm.

(including NO_2, NO and HONO) production rate is about 27.5 ppm/s inside the chamber volume under the conditions in Fig. 2.

Four different types of wire mesh; stainless steel (SS), stainless steel coated with WO_3 (SS + WO_3), copper (Cu), and tungsten (W) are investigated as electrode materials. Copper, tungsten and stainless steel are common electrode materials and WO_3 is a known catalyst for nitrogen fixation coated on the electrode to exploit the large contact area between the discharge and the mesh [44]. Fig. 3 shows the measured energy cost of NO_x production by DBD using the different mesh material under different discharge power densities. We observe no apparent difference in energy efficiency with different mesh materials used, under the near room-temperature conditions we studied. In other words, no catalytic effect appears to be present in the mesh. The energy cost of NO_x production tends to increase with increasing power in the range of 4000 GJ/tN–10,000 GJ/tN.

DBD is an attractive source for NO_x production, especially for combination with catalysis due to its large discharge area. However, we have found the energy cost of NO_x production with DBD is prohibitively high, compared to both the theoretical limit and other results reported in the literature using different types of discharges. For example, Patil et al. [28] report the energy cost of NO_x synthesis in the range of 3850 GJ/tN–5161 GJ/tN in a packed DBD reactor without catalyst. This
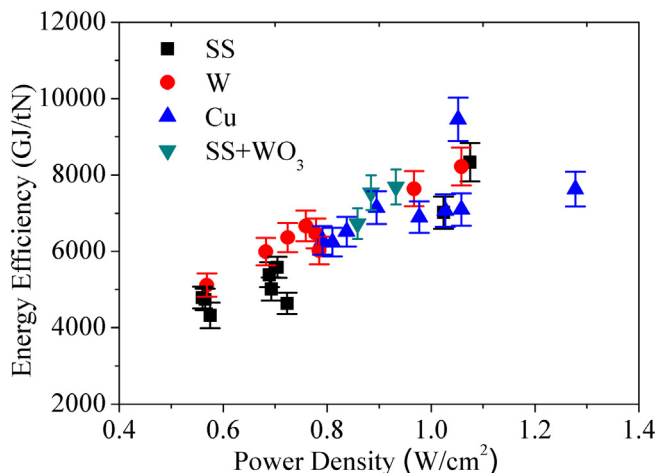

Fig. 3. Calculated energy cost (GJ/tN) of NO_x production in DBD with different mesh materials plotted as a function of power density.
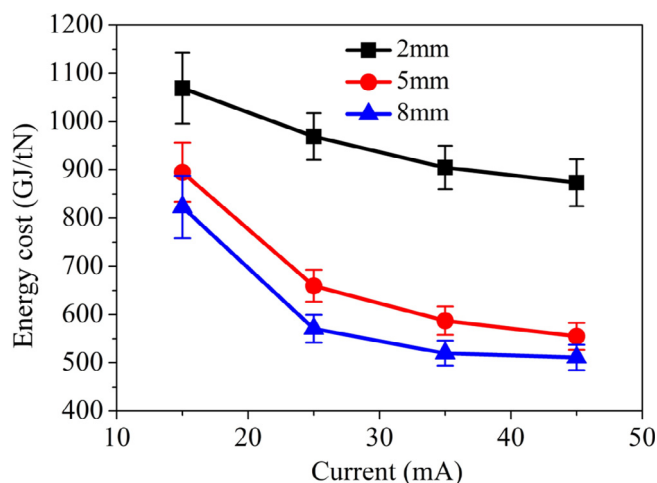
Fig. 4. Calculated energy cost (GJ/tN) for NO_x production in the DC glow discharge as a function of discharge current at different gap distances.
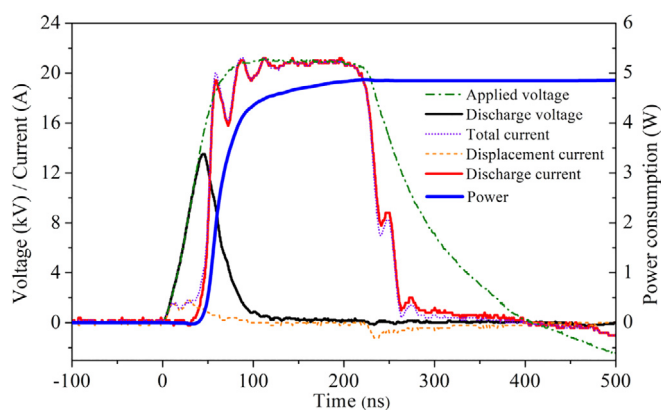

Fig. 5. Voltage and current observed in the nanosecond pulsed pin-to-plane discharge and the calculated power over a single pulse. Applied voltage is 20 kV, pulse width is 220 ns and gap distance is 5 mm.

result is similar to our results shown in Fig. 3. Notably, the measured gas temperature in the DBD is low (~400 K) which might be the reason for the absence of a catalytic effect in our experiments. Moreover, at low gas temperatures we observe a relatively high N_2O concentration as is seen in Fig. 2. These limitations severely impede the potential for DBD for energy-efficient NO_x fixation applications, compared to the warmer plasma sources we report on in the following sections.

3.2. NO_x production by DC glow discharge

We next investigate the DC glow discharge. For this source, we observe a constant discharge current and voltage throughout operation. Here, we investigate the energy cost for NO_x production at different gap distances and changing with the discharge current. Corresponding results are shown in Fig. 4. Notably, the energy cost decreases with increasing current (proportional to the discharge power) in the range of 15 mA–45 mA at all three different gap distances (2 mm, 5 mm, 8 mm). There also appears to be an inverse trend between the gap distance and the energy cost, with lower energy costs observed at the highest separation distance. A key characteristic of the glow discharge is the comparatively high gas temperatures observed. The average temperature $\overline{T}$ reaches 1500 ± 100 K–1800 ± 100 K as current is increased from 15 mA to 45 mA. However, the gap distance was found to only have a weak effect on $\overline{T}$ at a given current.

Overall, the energy cost of NO_x production is about an order of magnitude lower in the DC glow discharge than what is observed for the DBD. This points to the potential importance of the higher gas temperature in the discharge gap for efficient NO_x production. While the thermal effects might explain, in part, the decreased energy cost we observe with increasing current, it does not explain the effect of separation distance. A potential explanation may be found in the electrical properties of the discharge, which we probe in the next section using the pin-to-plane ns-pulsed spark discharge.

3.3. NO_x production by spark discharge

For the spark discharge we utilize a ns-pulsed power supply which allows access to relatively short timescale discharge dynamics. Using this set-up we study the effect of applied voltage, gap distance and pulse width on the energy cost of NO_x production. We present in Fig. 5 the time-resolved voltage and current profiles over a single pulse of the pin-to-plane discharge. Here, the applied voltage is set to 20 kV with a pulse width of 220 ns and a separation distance d of 5 mm. For the results reported in Fig. 5, and all the following results, the discharge frequency is fixed at 1 kHz. Since the utilized ns-power supply is a push-pull type,

the discharge voltage (gap voltage) is calculated as the difference between the measured voltages from two HV probes in the anode and cathode lines (see Fig. 1c). In order to calculate the discharge conduction current (corrected for propagation time delay, see Section 2.2.2), the displacement current is recorded with the discharge gap filled with dielectric oil (no discharge inside the gap).

To determine the discharge conduction current, the displacement current was subtracted from the total current (shown by the solid red line in Fig. 5). From Fig. 5, we observe that the discharge voltage initially increases up to about 14 kV when the air in the gap breaks down and the discharge current sharply rises. Due to the presence of a 1 kΩ current-limiting ballast resistor inside the power supply, the discharge current saturates at about 20 A. As the current rises, the discharge voltage quickly drops to a few hundred V. The time-resolved power consumption in the discharge is also presented in Fig. 5. Under these experimental conditions, the total plasma power consumption is 4.8 W. We observe, however, that most of the power is dissipated during the breakdown period (first 100 ns).

The average gas temperatures $\overline{T}$ are estimated by discharge OES at different experimental conditions (varying gap distance and pulse width with frequency fixed at 1 kHz). Over the experimental conditions we investigated, we find the value of $\overline{T}$ close to 550 ± 50 K. This can be explained by the fact that the time scale for gas heating (typically ~ few ms) is much larger than the pulse width we used here (max 260 ns). Although the current peak reaches 20 A, there is not enough time for the gas to heat during the pulse. Also the low frequency of 1 kHz leads to weak heat accumulation between each discharge period.

Fig. 6 shows the calculated energy cost for NO_x production in the pin-to-plane spark discharge as a function of pulse width at different applied voltage amplitudes (Fig. 6)) and different gap distances (Fig. 6(b)). In Fig. 6(a), the energy cost at all three applied voltage conditions (12 kV, 16 kV and 20 kV) decrease with increasing pulse width in the range of 100 ns–260 ns. The separation distance is fixed at 5 mm. The specific energy cost also decreases with increasing applied voltage at the same pulse width. In Fig. 6(b), three different gap distances (2 mm, 5 mm and 8 mm) are also investigated. The smaller gap distance is clearly shown to have the lower energy cost of NO_x production. This result is the inverse of what was observed for the DC glow discharge (see Fig. 4). We attribute this discrepancy to differences in the transient electric fields between the two discharges. Further discussion of this effect is provided in Section 3.5. Overall, the energy cost of NO_x production in the spark discharge is in a similar range with what is observed for the DC glow discharge. A slightly lower energy cost is observed with the spark discharge, for smaller d and a larger pulse width.

From Fig. 5 we note that most of the power is dissipated during the breakdown period (first 100 ns). This implies that the NO_x production
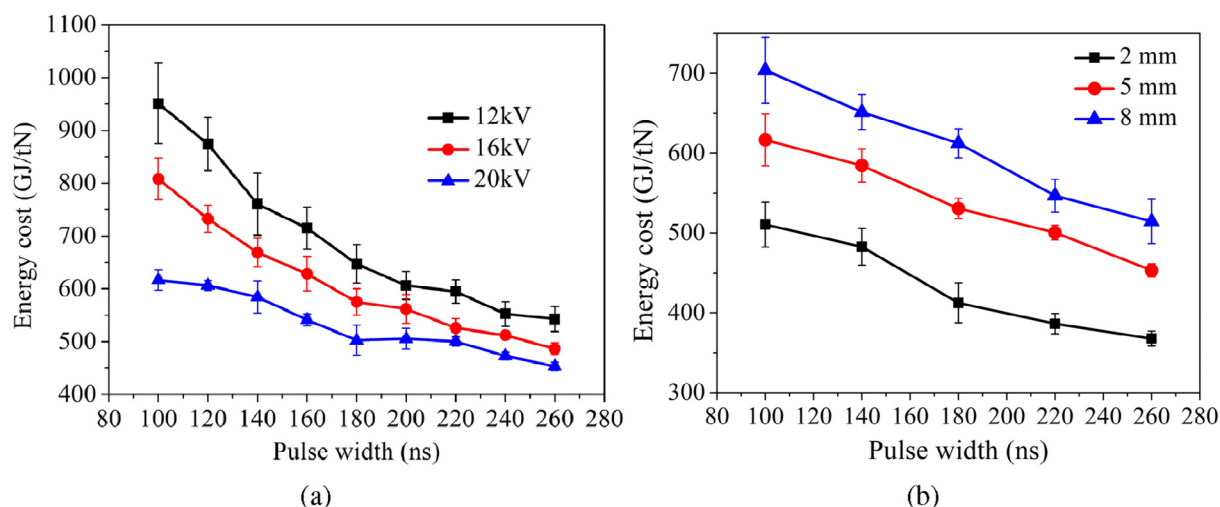
Fig. 6. Calculated specific energy cost (GJ/tN) for NO_x production in the pin-to-plane discharge as a function of pulse width at (a) different applied voltage amplitudes and (b) different gap distances.

energy cost during breakdown is higher than it is late in the pulse.

To further illustrate this point, we divide the discharge pulse into three regions (A, B, C). Identical profiles of gap voltage are measured with different pulse widths. The discharge current remains stable and reproducible as a function of pulse width, as seen in Fig. 7. We define the first region A to be the first 100 ns of the discharge. This includes the gas breakdown period, characterized by a sharp increase in current and decay in gap voltage. The current is maintained at its peak value, limited by the power supply as the voltage continues to decrease through the second region (B, 100–180 ns) and third region (C, 180–260 ns). The measured characteristics associated with each of these periods of time through the pulse are summarized in Table 2.

Based on the data presented in Table 2, by means of subtraction, we can obtain energy cost and rate of NO_x production corresponding to each region of time (A, B, C) during the pulse. For example, the power consumption for a pulse length of 260 ns is calculated as 4.00 W, 0.72 W and 0.20 W at regions A, B and C, respectively. Here, power is calculated as the product of energy consumed during the pulse (time integral of voltage and current) and the pulse frequency of 1 kHz, as described in Eq. (2) Similarly, using the FTIR measurements at the different pulse widths, we can calculate the corresponding NO_x production rates as 10.75 ppm/s, 4.97 ppm/s and 2.48 ppm/s for regions A, B, and C, respectively. This allows us to obtain NO_x production energy cost during these 3 regions: 638 GJ/tN, 248 GJ/tN and 138 GJ/tN. These are illustrated in Fig. 7.

Table 2

Discharge characteristics at different pulse widths, used to calculate properties of the different regions. Applied voltage 20 kV, frequency 1 kHz, gap distance 5 mm and chamber volume 1 L.

Pulse Width (ns)	100	180	260
Power Consumption (W)	4	4.72	4.92
NO_x production rate (ppm/s)	10.75	15.72	18.20
Energy Cost (GJ/tN)	638	514	463

Most significantly, we see that the majority of the energy consumption occurs during region A, which is associated with the breakdown process and a low energy efficiency. The NO_x production energy cost declines significantly during region B. Specific energy cost during the last region C is lower still.

One major implication of this analysis pertains to the energy cost associated with gas breakdown. The key conclusion is that NO_x production efficiency can be increased through making gas breakdown more efficient, i.e, by spending less energy on breakdown. In fact, as seen in Fig. 6(b), decreasing the separation distance drives down the cost of breakdown. This is associated with increased NO_x production efficiency. This observation might provide an explanation for the comparatively low energy cost for NO_x production reported with gliding arc (GA) discharges [29]. The discharge structure of the GA allows for ignition at a smaller gap, lowering the breakdown cost, and subsequent extension of the discharge improving efficiency. This
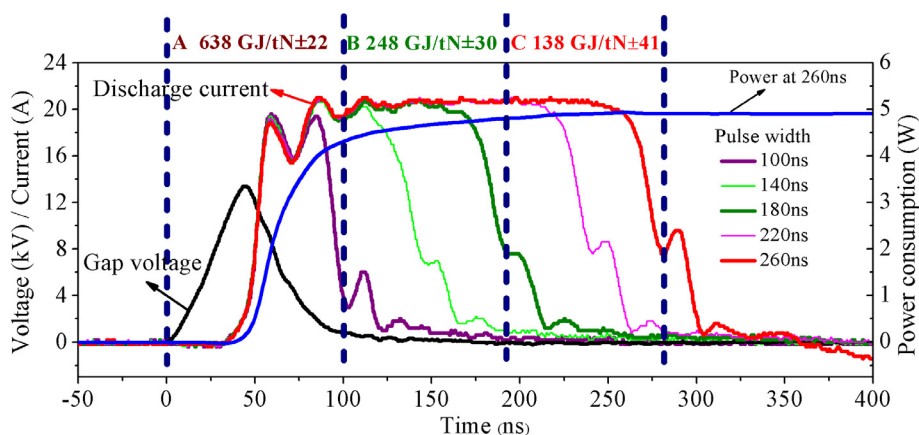

Fig. 7. Voltage-current characteristics of the spark discharge with different pulse widths. NO_x production energy cost is indicated at three different regions A, B and C. Region A includes breakdown and incurs the highest specific energy costs.
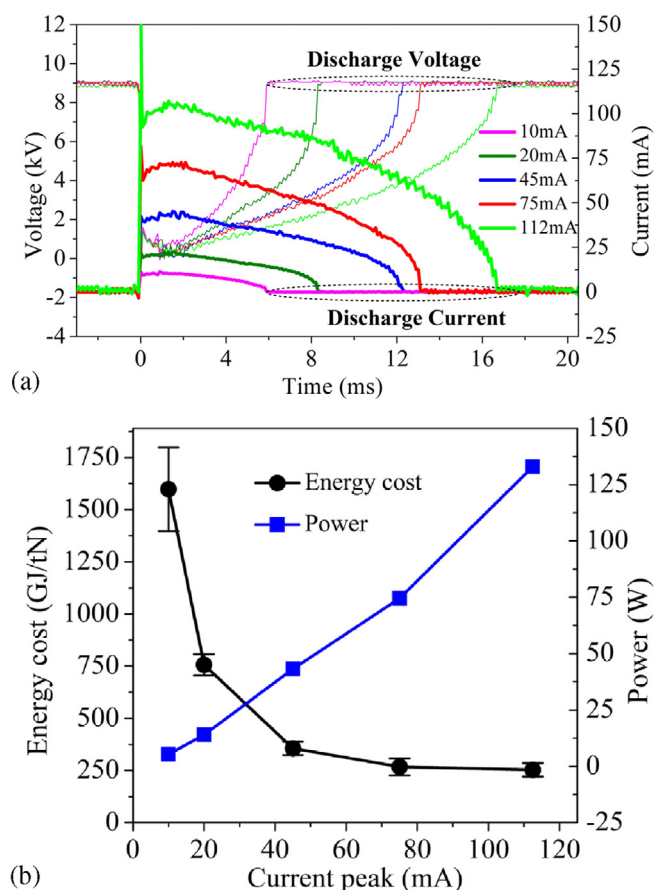
Fig. 8. (a) PA discharge voltage-current characteristics and, (b) energy cost (GJ/tN) and power consumption vs discharge current peak.

finding motivated our investigation of the extending-arc type PA discharge we discuss in the next section.

3.4. NOₓ production by PA discharge

PA is a novel type of atmospheric-pressure non-equilibrium discharge which relies on the rotation of the electrodes to extend the plasma length during operation. It is similar to the GA, in the sense that the breakdown occurs at a small gap distance when the propeller blades are close to the powered electrode and the discharge extends as the propeller rotates. A detailed characterization of the PA discharge is available in [42]. We investigate the effect of the current peak and ratio of N_2/O_2 in the chamber on the energy cost of NO_x production.

For the PA, a series of high power ballast resistors (80 kΩ, 120 kΩ, 200 kΩ, 450 kΩ and 900 kΩ) are used to limit the glow discharge current peak to 112 mA, 75 mA, 45 mA, 20 mA and 10 mA, respectively. Fig. 8(a) shows the waveform of PA discharge voltage and current using the different ballast resistors at the same applied voltage of 9 kV and controlled discharge frequency of 45 Hz. PA discharge is ignited by the breakdown region which is similar to a 'Transient Spark' and then the discharge mode transforms into a glow discharge due to the ballast resistor limitation. We observe that the discharge is extinguished earlier when a larger ballast resistor (corresponding to a smaller current peak) is used. When the discharge current peak is 112 mA, the sustaining time of PA reaches to 16.7 ms, which means the PA length can extend to about 8.2 cm ($\pi \times 3.5$ cm $\times 0.0167$ s $\times 45$ Hz). As the current peak decreases, the PA length becomes progressively shorter. At the discharge current peak of 10 mA, the PA length extends to only about 2.9 cm ($\pi \times 3.5$ cm $\times 0.0058$ s $\times 45$ Hz). For PA discharge, the $\overline{T}$ is observed to change in the range of 1300 K–1500 K with increasing
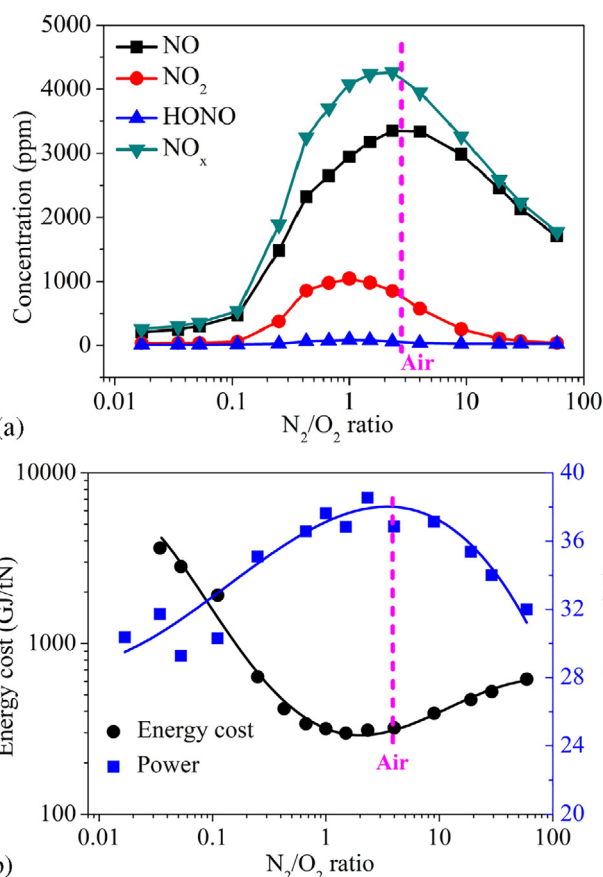

Fig. 9. Effect of the N_2/O_2 ratio to (a) the NO_x concentration and (b) the discharge power consumption and energy cost of NO_x production. The gas flow is 3 L/min and the applied voltage is 9 kV with a ballast resistor of 200 kΩ. The discharge frequency is fixed at 45 Hz.

current.

The effect of PA discharge current on the discharge power and energy cost for NO_x production is summarized in Fig. 8(b) under the same experimental conditions as in Fig. 8(a). The PA power consumption increases almost linearly with the current peak. The power consumption is only 5.4 W while the current peak is 10 mA, however, when the current peak is 112 mA, the discharge power increases to 133 W. The energy cost for NO_x production decreases drastically with the increasing current peak (or power consumption) and tends to a saturation value at about 253 GJ/tN. This is the lowest energy cost that we measured across the different types discharges investigated in this study.

As the PA appears to be relatively promising, we decided to explore additional parameters to decrease the NO_x production cost. The source of the produced NO_x in the plasma is the ambient N_2 and O_2 which corresponds to a fixed 3.71 ratio N_2/O_2. However, previous results [29] show that the N_2/O_2 ratio can have a significant impact on energy cost of NO_x production. Fig. 9 shows the effect of the N_2/O_2 ratio to the NO_x concentration and the energy cost of NO_x production for the PA discharge for an applied voltage of 9 kV and with current peak of 45 mA. The N_2/O_2 ratio is varied between 0.015 and 60 while maintaining a constant total gas flow of 3 L/min. The pink dashed line denotes the composition of ambient air. Based on Fig. 9(a), the total NO_x concentration (green triangles) shows that a N_2/O_2 ratio of 2 leads to the maximum NO_x concentration of 4462 ppm.

The power consumption (blue squares) of PA discharge is shown in Fig. 9(b) as a function of N_2/O_2 ratio. Although the applied electrical parameters (applied voltage, frequency, ballast resistor) are the same, the discharge power changes considerably (from 30 W to 38 W). The energy cost (black circles in Fig. 9(b)) reaches up to 2500 GJ/tN when

the N_2/O_2 ratio is 0.015. With the increase of N_2/O_2 ratio from 0.015 to 2, the NO_x production energy cost decreases to the lowest value of 300 GJ/tN at the N_2/O_2 ratio of 2. We notice that the energy cost is about 340 GJ/tN for the ambient air which is only 13% higher than the lowest value. As the N_2/O_2 ratio increases, the energy cost increases to 620 GJ/tN at N_2/O_2 ratio of 60.

3.5. Average electric fields

As noted above, decreasing the energy cost for NO_x production is a crucial objective for nitrogen fixation research. In this paper, we investigated 4 typical gas discharges; DBD, DC glow, spark and propeller arc for NO_x production from air. We found that the DBD appears to not be suitable for NO_x production from the view point of energy cost. The NO_x production energy cost in the DBD (4000 GJ/tN–10,000 GJ/tN) is at least an order of magnitude larger than the other discharges investigated in this study. A significant complication for the DBD nitrogen fixation is the abundant production of the greenhouse gas N_2O.

We therefore focus our discussion in the rest of the paper to the three remaining discharges. In order to obtain a common metric for the comparison of the DC glow, spark and PA discharges, we compute the average electric field for each discharge as described in Section 2.2.3.

Fig. 10 shows time-varying V_{dis}/d for the spark (Fig. 10(b)), and PA discharges (Fig. 10(c)) at different experimental conditions. For the DC glow discharge (Fig. 10(a)) since voltage is constant over time, the V_{dis}/d values are presented as a function of current.

For the DC glow discharge, V_{dis}/d decreases slightly with the increasing of current at all three gap distances. Naturally, the shorter gap distance, the higher V_{dis}/d which, in the case of the DC glow, is equal to $\overline{E}$. V_{dis}/d is presented for the spark discharge in Fig. 10(b) for an applied voltage of 20 kV and pulse width of 260 ns for three gap distances. We observe V_{dis}/d exhibits a peak with increasing pulse width of 75 ns, 105 ns and 150 ns for 2 mm, 5 mm and 8 mm gap distance, respectively. The 2 mm gap distance has the highest V_{dis}/d value at ~31.5 kV/cm and the earliest breakdown time t_{bre} of 25 ns compared to the larger gap distances. We note that although the V_{dis}/d decreases sharply after breakdown, it still maintains a value around several hundred kV/cm before the applied voltage is off (see Fig. 5). From Fig. 10(b) the time-averaged electric fields $\overline{E}$ are estimated to be 2.9 kV/cm, 3.3 kV/cm and 4.0 kV/cm for 2 mm, 5 mm and 8 mm, respectively. We note that the 2 mm gap distance has the minimum $\overline{E}$ even though it has the highest V_{dis}/d peak. This points to an inverse trend of $\overline{E}$ with gap distance, compared to the DC glow discharge. This inverted trend in $\overline{E}$ may provide an explanation to the inverse trend observed for energy cost with gap distance (see Figs. 4 and 6), between the DC glow and spark discharges.

For the PA discharge, time-resolved V_{dis}/d is presented in Fig. 10 (c). At the current peak of 112 mA, V_{dis}/d first increases to a peak of ~5 kV/cm at ~1.8 ms after the discharge ignition from ~1.2 kV/cm. After this peak value, corresponding to the minimum gap position of PA, V_{dis}/d decreases quickly to about 0.67 kV/cm at 5 ms (d ~2.5 cm) and maintains this relatively stable value up to ~15 ms (d ~7.4 cm) with a slight rise at the end at 17 ms. For other current peaks (10 mA, 20 mA, 45 mA and 75 mA), the V_{dis}/d have a similar trend as shown in Fig. 10(c). However, we observe that the higher current peak corresponds to lower average values of V_{dis}/d.

In order to better correlate $\overline{E}$ and energy cost for NO_x production at these three different discharges, we plot all the results of Fig. 4, Fig. 6, and Fig. 8 together as the function of $\overline{E}$ as shown in Fig. 11. One clear conclusion is that the energy cost, for each discharge type, tends to increase with increasing of $\overline{E}$. We note the results for the spark discharge (black triangles), do not follow the general correlation for the DC glow and PA, although the increasing trend between $\overline{E}$ and energy cost is preserved. $\overline{E}$ appears to be an important parameter to correlate the results we have collected, but it notably does not contain information about the thermal effects. In the next section we include the
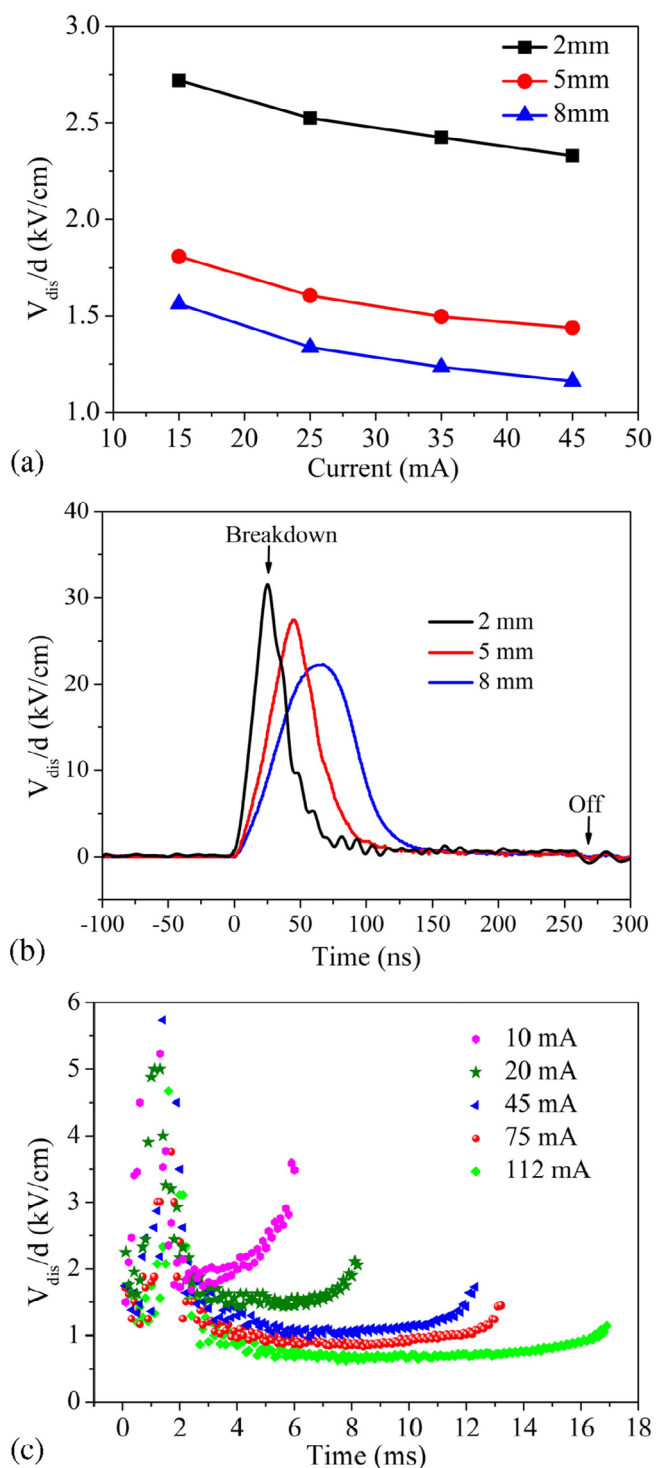

(a)

(b)

(c)

Fig. 10. The real-time V_{dis}/d change for (a) glow, (b) spark and (c) PA discharge at different experiment conditions.

thermal effects to come up with a single parameter that correlates all of the results.

3.6. The χ factor

During our experiments, we found that the gas temperatures for each discharge are significantly different. To further analyze the NO_x production of different discharges, we bring the gas temperature into consideration and define the dimensionless parameter χ as follows:
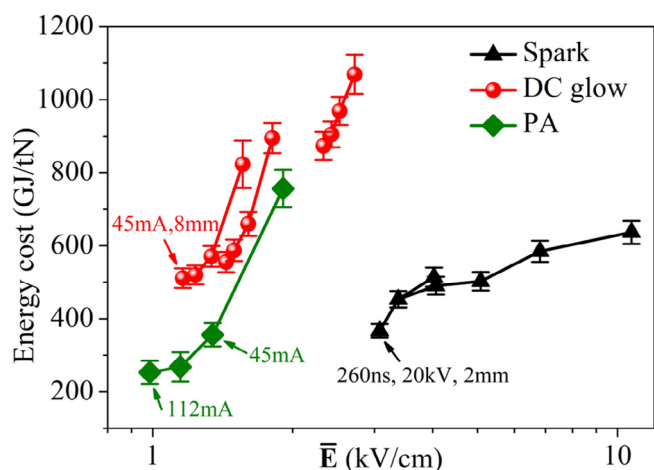
Fig. 11. Energy cost for NO_x production in spark, glow and PA discharge with different conditions plotted as a function of $\overline{E}$.

$$\chi = \frac{\overline{E} \times \overline{T}}{E_r \times T_r} \tag{6}$$

where $\overline{E}$ is calculated from (4) with units of kV/cm; $\overline{T}$ is the average temperature mentioned in Section 2.2.4 with units of K; E_r and T_r are chosen to normalize the parameter at a reference condition. We choose (somewhat arbitrarily) the DC glow discharge with a gap distance of 5 mm and a discharge current of 45 mA as this reference condition. Since DC glow discharge has a simple and stable discharge character, the discharge conditions can be replicated easily for reference. The corresponding values of E_r and T_r 1.43 kV/cm and 1800 K respectively.

We also compute corresponding values of χ and NO_x production costs from the literature. We include results corresponding to region C for our spark discharge (see Fig. 7). We note here that region C does not represent an independent condition on its own and is necessarily preceded by a less efficient breakdown process. We summarize the collected data in Table 3. Fig. 12 shows how the energy cost for NO_x production varies with χ for the different types of discharges. Remarkably, there is an almost linear relationship between χ and energy cost for NO_x production. We provide the linear fit for the data in Fig. 12, expressed by

$$y = Ax + B. \tag{7}$$

We compute the coefficients in (7) to be $A = 450 \pm 41$ GJ/tN and $B = 124 \pm 49$ GJ/tN. The region of 95% confidence interval based on Table 3 is shown in Fig. 12 via the two dashed lines. The coefficients A and B have some physical meaning. Value of A indicates that per unit decrease in χ we expect the energy cost to decrease by about 450 GJ/
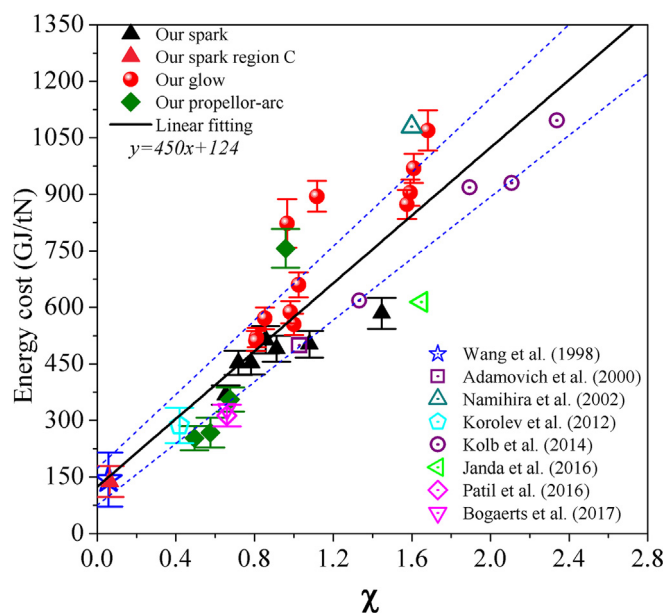

Fig. 12. Energy cost for NO_x production vary with χ based on the reported works and our results using different plasma sources.

tN. The value of the intercept B provides an estimate for the lower limit of energy cost for NO_x production at about 124 ± 49 GJ/tN. We note that this value is particularly close to the energy cost associated with region C (138 GJ/tN). Note here that all the data provided in Table 3 correspond to discharges at atmospheric pressure. We expect the relationship between χ and energy cost to change under varying pressure conditions, although that relationship has not been addressed here.

We notice that the χ factor seems related to the parameter reduced electric field E/N (E is the electric field strength, N is the gas density). The gas density N during discharge is generally difficult to measure due to simultaneous variations in gas pressure and gas temperature. Another key consideration is the transient and spatially distributed characteristics of E/N in these discharges. In fact, period-averaged E/N values corresponding to the lowest values of χ in Fig. 12 would be too small to excite the key reactions for NO_x production, including N_2 dissociation. Therefore χ appears to be a more convenient metric.

3.7. Energy cost reduction guidelines by the χ factor

Surprisingly, the χ factor, as defined in (6), correlates with the energy cost of NO_x production for strikingly different types of discharges. This suggests χ captures some implicit time and space dependent phenomena that must govern NO_x production in air discharges.

Table 3
Summary of NO_x production based on the reported works and our results using different plasma sources.

d (cm)	V_{dis} (kV)	Current Peak (A)	Pulse Width (μs)	$\overline{T}$ (K)	GJ/tN	Ref.
0.2–0.8	0.64–3.2	20	0.26	500–600	367–584	Spark
0.5	0.15	20	0.1	550	138±41	Region C
0.2–0.8	0.46–1.25	0.015–0.045	DC	1500–1800	511–1069	DC glow
0.05–8.5	0–9	0.02–0.112	8200–16700	1300–1500	253–756	PA
3.2	0.032	19000	430	15000	143±70	Wang [17]*
5	0.7	0.04	DC	1750	500	Adamovich [22]**
0.5	0.207	1000	3	10000	1080	Namihiraet [23,24]***
1	0.903	0.2	DC	1200	286±50	Korolev [26]
0.08	0.27–0.52	0.02–0.05	DC	1000	617–1096	Kolb [27]
0.6	2.56	15	0.02	1000	614	Janda [30]
0.13–1.37	1.09	AC 0.2	70	1250	330, 285–342	Patil and Bogaerts [33,29]

* V_{dis} was estimated from the discharge energy and discharge current peak of 19 kA.

** $\overline{T}$ and GJ/tN come from simulation results of 40 mA.

*** V_{dis} was estimated from plasma resistance.

The mechanisms for NO_x formation are not fully understood, so our interpretation of the significance of the χ factor is correspondingly uncertain. However, we can make some educated guesses about possible mechanisms.

The energy efficiency of NO_x production in discharges is commonly attributed to one or both of two mechanisms [12]: (i) efficient electron-impact activation of N_2 to facilitate NO_x formation and (ii) rapid thermal quenching of NO to prevent its conversion back to N_2 and O_2 as gas temperature is lowered. Activation of N_2 through electron-impact induced electronic [35,45,46] or vibrational [29] excitation can help accelerate the often rate-limiting step of N_2 dissociation. The rapid quenching of plasma species helps arrest the non-equilibrium discharge chemistry to form desirable products [47]. The χ factor could be relevant to both of these mechanisms. The average electric field $\bar{E}$ influences the rates of electron-N_2 excitation, thereby influencing energy transfer to both electronic and vibrational levels. Furthermore, the gas temperature $\bar{T}$ is likely related to the thermal gradient across which the discharge products are quenched.

Based on the trend we observe in Fig. 12, reducing the χ factor, while sustaining the discharge, can be a guiding principle for reducing the energy cost of NO_x production. However, decreasing the χ factor is not necessarily straightforward. $\bar{E}$ and $\bar{T}$ are often correlated in any particular discharge, and they cannot generally be directly manipulated. The applied voltage and the discharge (gap) voltage are not the same. The discharge voltage is a consequence of the gap distance, power supply characteristics and external circuit properties. Similarly, $\bar{T}$ varies with the electrical and thermal properties of the discharge. Higher currents which correspond to a lower $\bar{E}$ typically lead to an increase in $\bar{T}$.

Some of the published recommendations for increased energy efficiency of NO_x production in the literature coincide with decreasing the value of the χ parameter. For example, extending the plasma length during operation as suggested in several papers [5,48,29,33], can reduce the χ factor. We demonstrated this effect in our investigation of the PA. Another solution is to cool the discharge area or the electrodes with gas flow or with a cooled adjacent surface [49]. This effect might be related to enhanced thermal quenching of NO. With cooling at constant pressure, and assuming no change in $\bar{E}$, we would obtain a lower χ. Finally, the timescale separation between electrical (~ns) and neutral gas transport phenomena (~ms-s) could be exploited to increase energy efficiency. A low gas temperature can be maintained at a high current discharge through application of short duration (ns-ms) pulsed power, leading to a lower χ value. We observe this effect in the ns-pulsed spark discharge. In Fig. 7 region C has a very low χ factor (~0.06), due to the high discharge current (20 A) corresponding to a low $\bar{E}$ and extremely short discharge pulse (260 ns). This prevents $\bar{T}$ from increasing during the discharge pulse. However, in practice this condition is necessarily preceded by gas breakdown, with a considerably larger χ factor, thereby leading to a higher energy cost overall. The χ factor represents a conveniently measured metric for quantifying and improving the energy efficiency of NO_x production.

4. Concluding remarks

Increasing the energy efficiency of nitrogen fixation using air plasmas should significantly advance their use as a novel technology to reduce the deleterious environmental impacts of growing fertilizer demand on the global nitrogen cycle. In this paper, we investigated the energy cost of NO_x production using four types of discharges: DBD, glow, spark and PA in air.

Based on the results we presented here, we found the two key parameters controlling NO_x production efficiency to be the average electric field $\bar{E}$ and average gas temperature $\bar{T}$. Using these parameters we define the dimensionless parameter χ, the normalized product of $\bar{E}$ and $\bar{T}$. This quantity appears to effectively correlate specific energy cost of NO_x production for the discharges we studied as well as results from

the literature. Based on our results we conclude that reducing χ could be a guiding principle in designing sources for energy-efficient NO_x production.

We suggest several methods to reduce χ by reducing the plasma gas temperature by cooling or using short duration, high current pulses or by extending the discharge length. The effects of these suggestions have been demonstrated by our experiments and/or reported in the literature. The χ factor appears to serve as a simple, effective means of correlating NO_x production energy efficiency across a broad range of discharges. This indicates that χ captures some intrinsic, but still poorly understood, physical and/or chemical mechanisms governing NO_x production. Future research should focus on revealing these intrinsic mechanisms to further improve the practical attractiveness of air plasma for nitrogen fixation.

References

[1] Y. Tanabe, Y. Nishibayashi, Developing more sustainable processes for ammonia synthesis, Coord. Chem. Rev. 257 (17–18) (2013) 2551–2564.

[2] N. Cherkasov, A. Ibhadon, P. Fitzpatrick, A review of the existing and alternative methods for greener nitrogen fixation, Chem. Eng. Process. 90 (2015) 24–33.

[3] J.G. Chen, R.M. Crooks, L.C. Seefeldt, K.L. Bren, R.M. Bullock, M.Y. Darensbourg, P.L. Holland, B. Hoffman, M.J. Janik, A.K. Jones, M.G. Kanatzidis, P. King, K.M. Lancaster, S.V. Lymar, P. Pfromm, W.F. Schneider, R.R. Schrock, Beyond fossil fuel-driven nitrogen transformations, Science 360 (6391) (2018).

[4] V. Smil, Energy in Nature and Society: General Energetics of Complex Systems, MIT Press, Cambridge, Massachussetts, 2008.

[5] B. Patil, Q. Wang, V. Hessel, J. Lang, Plasma N2-fixation: 1900–2014, Catal. Today 256 (2015) 49–66.

[6] V. Smil, Nitrogen and food production: proteins for human diets, J. Human Environ. 31 (2) (2002) 126–131.

[7] M.A. Sutton (Ed.), Our Nutrient World: The Challenge to Produce more Food and Energy with Less Pollution; [Global Overview on Nutrient Management], Centre for Ecology & Hydrology, Edinburgh, 2013.

[8] J.G. Chen, R.M. Crooks, L.C. Seefeldt, K.L. Bren, R.M. Bullock, M.Y. Darensbourg, P.L. Holland, B. Hoffman, M.J. Janik, A.K. Jones, M.G. Kanatzidis, P. King, K.M. Lancaster, S.V. Lymar, P. Pfromm, W.F. Schneider, R.R. Schrock, Inorganic chemistry beyond fossil fuel-driven nitrogen transformations, Science 360 (6391) (2018) 873.

[9] W. Steffen, K. Richardson, J. Rockstrom, S.E. Cornell, I. Fetzer, E.M. Bennett, R. Biggs, S.R. Carpenter, W. de Vries, C.A. de Wit, C. Folke, D. Gerten, J. Heinke, G.M. Mace, L.M. Persson, V. Ramanathan, B. Reyers, S. Sorlin, Planetary boundaries: guiding human development on a changing planet, Science 347 (6223) (2015) 1259855.

[10] J.N. Galloway, J.D. Aber, J.W. Erisman, S.P. Seitzinger, R.W. Howarth, E.B. Cowling, B.J. Cosby, The nitrogen cascade, Bioscience 53 (4) (2003) 341.

[11] A.S. Travis, The Synthetic Nitrogen Industry in World War I. SpringerBriefs in Molecular Science, Springer International Publishing, Cham, 2015.

[12] R. Ingels, D.B. Graves, Improving the efficiency of organic fertilizer and nitrogen use via air plasma and distributed renewable energy, Plasma Med. 5 (2–4) (2015) 257–270.

[13] D.B. Graves, L.B. Bakken, M.B. Jensen, R. Ingels, Plasma activated organic fertilizer, Plasma Chem. Plasma Process. (2018), https://doi.org/10.1007/s11090-018-9944-9.

[14] W.L. Chameides, D.H. Stedman, R.R. Dickerson, D.W. Rusch, R.J. Cicerone, Nox production in lightning, J. Atmospheric Sci. 34 (1) (1977) 143–149.

[15] R.D. Hill, R.G. Rinker, D. Wilson, Mechanism of nox production by lightning, Trans.-Am. Geophys. Union 59 (12) (1978) 1077–1078.

[16] R. Navarro-Gonzalez, M. Villagran-Muniz, H. Sobral, L.T. Molina, M.J. Molina, The physical mechanism of nitric oxide formation in simulated lightning, Geophys. Res. Lett. 28 (20) (2001) 3867–3870.

[17] Y. Wang, A.W. DeSilva, G.C. Goldenbaum, R.R. Dickerson, Nitric oxide production by simulated lightning: dependence on current, energy, and pressure, J. Geophys. Res.-Atmospheres 103 (D15) (1998) 19149–19159.

[18] X. Tie, R. Zhang, G. Brasseur, W. Lei, Global NOx production by lightning, J. Atmos. Chem. 43 (1) (2002) 61–74.

[19] M.S. Stark, J.T.H. Harrison, C. Anastasi, Formation of nitrogen oxides by electrical discharges and implications for atmospheric lightning, J. Geophys. Res.: Atmospheres 101 (D3) (1996) 6963–6969.

[20] U. Schumann, H. Huntrieser, The global lightning-induced nitrogen oxides source, Atmospheric Chem. Phys. Discuss. 7 (1) (2007) 2623–2818.

[21] V. Cooray, M. Rahman, V. Rakov, On the no(x) production by laboratory electrical discharges and lightning, J. Atmos. Solar Terr. Phys. 71 (17–18) (2009) 1877–1889.

[22] I. Adamovich, W. Rich, P. Chernukho, S. Zhdanok, Analysis of the power budget and stability of high-pressure nonequilibrium air plasmas, in: 31st Plasmadynamics and Lasers Conference, vol. Denver, CO, U.S.A, 2000.

[23] T. Namihira, S. Katsuki, R. Hackam, H. Akiyama, K. Okamoto, Production of nitric oxide using a pulsed arc discharge, IEEE Trans. Plasma Sci. 30 (5) (2002) 1993–1998.

[24] T. Namihira, S. Sakai, M. Matsuda, D. Wang, T. Kiyan, H. Akiyama, K. Okamoto, K. Toda, Temperature and nitric oxide generation in a pulsed arc discharge plasma, Plasma Sci. Technol. 9 (6) (2007) 747–751.

[25] S. Sakai, M. Matsuda, D. Wang, T. Namihira, H. Akiyama, K. Okamoto, K. Toda, Nitric oxide generator based on pulsed arc discharge, Acta Phys. Pol. A 115 (6) (2009) 1104–1106.

[26] Y.D. Korolev, O.B. Frants, N.V. Landl, A.I. Suslov, Low-current plasmatron as a source of nitrogen oxide molecules, IEEE Trans. Plasma Sci. 40 (11) (2012) 2837–2842.

[27] X.L. Hao, A.M. Mattson, C.M. Edelblute, M.A. Malik, L.C. Heller, J.F. Kolb, Nitric oxide generation with an air operated non-thermal plasma jet and associated microbial inactivation mechanisms, Plasma Processes Polym. 11 (11) (2014) 1044–1056.

[28] B. Patil, N. Cherkasov, J. Lang, A. Ibhadon, V. Hessel, Q. Wang, Low temperature plasma-catalytic NO$_x$ synthesis in a packed DBD reactor: effect of support materials and supported active metal oxides, Appl. Catal. B: Environ. 194 (2016) 123–133.

[29] W. Wang, B. Patil, S. Heijkers, V. Hessel, A. Bogaerts, Nitrogen fixation by gliding arc plasma: better insight by chemical kinetics modelling, ChemSusChem 10 (10) (2017) 2145–2157.

[30] M. Janda, V. Martišovitš, K. Hensel, Z. Machala, Generation of antimicrobial NOx by atmospheric air transient spark discharge, Plasma Chem. Plasma Process. 36 (3) (2016) 767–781.

[31] M.A. Malik, Nitric oxide production by high voltage electrical discharges for medical uses: a review, Plasma Chem. Plasma Process. 36 (3) (2016) 737–766.

[32] M. Iwamoto, M. Akiyama, K. Aihara, T. Deguchi, Ammonia synthesis on wool-like au, pt, pd, ag, or cu electrode catalysts in nonthermal atmospheric-pressure plasma of n-2 and h-2, ACS Catal. 7 (10) (2017) 6924–6929.

[33] B.S. Patil, J.R. Palau, V. Hessel, J. Lang, Q. Wang, Plasma nitrogen oxides synthesis in a milli-scale gliding arc reactor: investigating the electrical and process parameters, Plasma Chem. Plasma Process. 36 (1) (2016) 241–257.

[34] C.Z.X.G. Jin Yang, Tianyue Li, C. Hu, Nitrogen fixation in water using air phase gliding arc plasma, J. Electrochem. Soc. 163 (10) (2016) E288–E292.

[35] D. Burnette, A. Montello, I.V. Adamovich, W.R. Lempert, Nitric oxide kinetics in the afterglow of a diffuse plasma filament, Plasma Sour. Sci. Technol. 23 (4) (2014) 045007 .

[36] Y.P. Raizer, Gas Discharge Physics, Springer-Verlag, 1991.

[37] M.J. Pavlovich, H.W. Chang, Y. Sakiyama, D.S. Clark, D.B. Graves, Ozone correlates with antibacterial effects from indirect air dielectric barrier discharge treatment of water, J. Phys. D-Appl. Phys. 46 (14) (2013).

[38] M.J. Pavlovich, Y. Sakiyama, D.S. Clark, D.B. Graves, Antimicrobial synergy between ambient-gas plasma and uva treatment of aqueous solution, Plasma Processes Polym. 10 (12) (2013) 1051–1060.

[39] M.J. Pavlovich, Z. Chen, Y. Sakiyama, D.S. Clark, D.B. Graves, Effect of discharge parameters and surface characteristics on ambient-gas plasma disinfection, Plasma Processes Polym. 10 (1) (2013) 69–76.

[40] M.J. Pavlovich, D.S. Clark, D.B. Graves, Quantification of air plasma chemistry for surface disinfection, Plasma Sour. Sci. Technol. 23 (6) (2014) pp.

[41] D.Z. Pai, D.A. Lacoste, C.O. Laux, Nanosecond repetitively pulsed discharges in air at atmospheric pressure-the spark regime, Plasma Sour. Sci. Technol. 19 (6) (2010).

[42] X. Pei, D. Gidon, D.B. Graves, Propeller arc: design and basic characteristics, Plasma Sour. Sci. Technol. (2018) (accepted).

[43] C.O. Laux, T.G. Spence, C.H. Kruger, R.N. Zare, Optical diagnostics of atmospheric pressure air plasmas, Plasma Sour. Sci. Technol. 12 (2) (2003) 125–138.

[44] I.M. Szilagyi, B. Forizs, O. Rosseler, A. Szegedi, P. Nemeth, P. Kiraly, G. Tarkanyi, B. Vajna, K. Varga-Josepovits, K. Laszlo, A.L. Toth, P. Baranyai, M. Leskela, Wo3 photocatalysts: influence of structure and composition, J. Catal. 294 (2012) 119–127.

[45] D. Burnette, I. Shkurenkov, I.V. Adamovich, W.R. Lempert, Kinetics of no formation and decay in nanosecond pulse discharges in air, h-2-air, and c2h4-air mixtures, Plasma Sour. Sci. Technol. 25 (2) (2016).

[46] I. Shkurenkov, D. Burnette, W.R. Lempert, I.V. Adamovich, Kinetics of excited states and radicals in a nanosecond pulse discharge and afterglow in nitrogen and air, Plasma Sour. Sci. Technol. 23 (6) (2014).

[47] Y.P. Tsui, H.Y. Cheh, Quenching of air plsma effluents, Plasma Chem. Plasma Process. 2 (4) (1982) 387–398.

[48] A.V. Grosse, E.W. Smith, Energy efficient process for producing nitrogen oxide, US Patent, no. US3666408A, 1972.

[49] R. Ingels, Energy efficient process for producing nitrogen oxide, *European Patent*, no. EP2704989B1, 2012.